Experimental Thermal and Fluid Science 85 (2017) 213–228

Contents lists available at ScienceDirect

Experimental Thermal and Fluid Science

journal homepage: www.elsevier.com/locate/etfs

Supersonic flow over rounded contour bumps with vortex generators or passive longitudinal jets

Kin Hing Lo *, Konstantinos Kontis

Division of Aerospace Sciences, School of Engineering, University of Glasgow, University Avenue, Glasgow G12 8QQ, United Kingdom

ARTICLE INFO

Article history:
Received 4 October 2016
Received in revised form 18 January 2017
Accepted 3 March 2017
Available online 6 March 2017

Keywords:
Contour bump
Flow control
Passive jet
Supersonic wind tunnel
Vortex generator

ABSTRACT

An experimental study has been conducted to investigate the flow characteristics over two rounded contour bumps. Vane-type vortex generators or longitudinal aligned passive by-pass jets were implemented in attempt to achieve wake flow control in rounded contour bumps. According to the results collected from the surface oil flow visualisation experiments, it was observed that the use of both the vane-type vortex generators and the longitudinally aligned passive by-pass jet could reduce the size of the spanwise vortices in the bump valley. In addition, a pair of streamwise horseshoe vortices was observed downstream of the bump crest of the contour bump that equipped with the vane-type vortex generators. From the data collected in the particle image velocimetry measurements, it was found that the use of both the vane-type vortex generators and the longitudinally aligned passive by-pass jet could not reduce the size of the wake region but they could reduce its strength. It is deduced that the two streamwise horseshoe vortices generated by the vane-type vortex generators enhance flow mixing which results in reducing the strength of the wake region. In contrast, blowing passive by-pass jet in the bump valley increases the local flow velocity in order to reduce the strength of the wake region.

1. Introduction

Flow characteristics over rounded contour bumps have been extensively investigated in both subsonic and supersonic freestream in the last two decades [1–8] because of their potential applications in achieving wave drag reduction in both transonic aircraft wings [9–13] and Diverterness Supersonic Inlets (DSI) [14,15]. In the flow physics of rounded contour bumps, the experimental studies conducted by Byun [1] and Byun et al. [2] were two earliest investigations in the flow characteristics over a range of three-dimensional rounded contour bumps in subsonic freestream. The authors in these studies observed that large-scale vortical structures are presented downstream of the bump crest due to the occurrence of flow separation at the leeward side of the bump. In addition, spanwise, counter-rotating vortices are formed in the valley of the rounded contour bumps resulting from flow separation. The authors concluded that the length-to-width and length-to-apex height ratios of the bump determine the number, size and shape of the spanwise vortices that present at the leeward side of a rounded contour bump.

Yakeno et al. [3] and Iaccarino et al. [4] considered the flow physics over two-dimensional rounded contour bumps in subsonic laminar and turbulent flow, respectively. The authors in [3,4] confirmed the conclusions drawn by Byun [1] and Byun et al. [2] that the appearance of flow separation at the leeward side of the bump leads to the formation of large-scale three-dimensional vortical structures downstream of the bump crest. Moreover, the authors indicated that the flow Reynolds number determines the size and shape of the vortical structures that formed. Long and wide vortical structures are presented when the rounded contour bumps are subjected to laminar flow. In contrast, the vortical structures those shown in turbulent flow are generally shorter and narrower. Svensson [15] investigated numerically the problem of subsonic flow over a number of three-dimensional rounded contour bumps with various length-to-width and length-to-apex height ratios. The author confirmed the formation of large-scale three-dimensional vortical structures and the spanwise counter-rotating vortices at the leeward side of the bump as concluded in [1–4]. In addition, the author observed that for a given length-to-width ratio of a rounded contour bump, in subsonic flow, increasing the freestream Mach number increases the sizes of both the wake region and the spanwise vortices that present at the leeward side of the bump. This further indicates that the size and shape of the flow features that formed are flow Reynolds number dependent.

* Corresponding author.
E-mail addresses: kinhing.lo@glasgow.ac.uk (K.H. Lo), kostas.kontis@glasgow.ac.uk (K. Kontis).

http://dx.doi.org/10.1016/j.expthermflusci.2017.03.005
0894-1777/

In supersonic flow, Lo [5], Lo and Kontis [6,7] and Svensson [15] studied the flow characteristics over three-dimensional rounded contour bumps. In the numerical study conducted by Svensoon [15], the author concluded that the large-scale three-dimensional vortical structures and the spanwise counter-rotating vortices that present in subsonic flow also appear in supersonic freestream. Interestingly, the author found that for a rounded contour bump with a given length-to-width ratio, the sizes of the three-dimensional vortical structures and the spanwise vortices reduce with increasing the freestream Mach number. This finding was later confirmed in the experimental study conducted by Lo [5] using a three-dimensional rounded contour bump subjected to both Mach 1.3 and 1.9 supersonic freestream. The author in [5] confirmed that larger wake region and spanwise counter-rotating vortices are formed at the leeward side of the bump in Mach 1.3 freestream than those shown in Mach 1.9 freestream.

Since flow separation is observed downstream of the bump crest of rounded contour bumps which leads to the formation of the wake region at the leeward side of the bumps; wake flow control in subsonic and supersonic freestream using various flow control strategies have been investigated in several studies [5–7,16,17]. Recently, Chen et al. [16,17] investigated the effects of passive jet in achieving wake flow control over a stationary circular cylinder in a subsonic freestream. The authors concluded that compared to the baseline circular cylinder, blowing passive-by-pass jet at the leeward side could effectively reduce drag encountered by the circular cylinder. In addition, the passive blowing jet reduces the turbulence kinetic energy levels along the wake region with passive jet blowing implemented at the leeward side of the circular cylinder.

Lo and Kontis [6] recently investigated the functions of transverse passive by-pass jet and active blowing jet in achieving wake flow control in a three-dimensional rounded contour bump in Mach 1.3 freestream. The authors in [6] found that the use of transverse passive by-pass jet could reduce neither the size nor the strength of the wake region. It was observed that the blowing transverse passive by-pass jet could only exert effects immediately behind the jet orifices that situated in the bump valley. However, the result shown in [6] suggested that the blowing transverse passive by-pass jet could reduce the size and strength of the spanwise vortices that formed in the bump valley by hindering the formation of the spanwise vortices around the centre portion of the bump. In contrast, the blowing active jet with total pressure of 2 and 4 bar in the bump valley could effectively reduce both the size and strength of the wake region at the leeward size of the bump in Mach 1.3 freestream. The authors in [6] indicated that the active blowing jet deflected the shear layer downwards so that reattachment of the separated flow downstream of the bump crest is accelerated. In addition, the active blowing jet in the bump valley also increases the momentum of the flow in the wake region so that the strength of the wake vortex is significantly reduced. This wake flow control effect is particularly promising when the jet total pressure is 2 bar. Moreover, the blowing jet also increases the local pressure level around the centre portion of the bump valley and hence, only small and diffuse spanwise vortices are formed in the bump valley. Similar effects provided by the active blowing jet in achieving wake flow control in three-dimensional rounded contour bumps also observed in Mach 1.9 freestream as concluded by Lo et al. [7]. However, the size and structure of the spanwise vortices that present in the bump valley in Mach 1.9 freestream are considerably different from those shown in Mach 1.3 freestream.

The present experimental study serves as the second part of an earlier study conducted by Lo and Kontis [6] in order to investigate the functions of vane-type vortex generators and longitudinally aligned passive by-pass jet in achieving wake flow control in three-dimensional rounded contour bumps in Mach 1.3 freestream. Vortex generators have been proven to be able to achieve flow separation control in transonic and supersonic freestream [18–22]. It is unclear that whether the same flow control strategy in achieving wake flow control can be achieved in three-dimensional rounded contour bumps. Similarly, it is also unclear that whether flow control in rounded contour bumps could be obtained by blowing longitudinally aligned passive by-pass jet in the bump valley as observed in [16,17] using a stationary circular cylinder. Surface oil flow visualisation, high-speed Schlieren photography and time-averaged two-component Particle Image Velocimetry (PIV) measurements were used for flow diagnostics. The data collected from the present study could improve our understanding in using vane-type vortex generators and passive by-pass jet in achieving wake flow control in three-dimensional rounded contour bumps.

2. Experimental setup

2.1. Supersonic wind tunnel

All experiments in the present study were conducted using an intermittent in-draft supersonic wind tunnel. A systematic diagram and a snapshot of the actual wind tunnel used are shown in Fig. 1a and b, respectively. Detailed information of the supersonic wind tunnel used could be found in [5–8] and only a brief description is provided here. The required Mach 1.3 free-stream was generated by expanding the incoming airflow through a convergent-divergent nozzle situated upstream of the wind tunnel test section. The contour bump model was mounted 82.5 mm downstream of the beginning of the wind tunnel test section. Optical access to the wind tunnel test section was achieved through the two quartz-made side windows and the ceiling mounted quartz window. The wind tunnel has a stable run-time of 6 s. Under the same initial conditions, the variation of the freestream Mach number (M_∞) is $M_\infty = 1.3 \pm 0.1$ [6,8] which is corresponding to the freestream velocity $U_\infty = 373 \pm 37\ ms^{-1}$. The inlet of the supersonic wind tunnel is subjected to atmospheric pressure and temperature. Static pressure (P) and temperature (T) in the test section during wind tunnel operation are P = 35.84 kPa and T = 203.79 K. The flow Reynolds number per unit length (Re/L) is $Re/L = 12.11 \times 10^6$ [6].

The boundary layer profile of the incoming flow 5 mm upstream of the front of the contour bump model was measured using a pitot rig and the detailed methodology of measurement could be found in [6]. At that location, the boundary layer thickness based on 99% of the freestream velocity (δ_{99}) is 14.9 mm. The corresponding displacement (δ^*) and momentum thickness (θ) of the boundary layer are $\delta^* = 4.54$ mm and $\theta = 2.57$ mm. This yields a shape factor (H), defined as the ratio between δ^* and θ, of H = 1.77. Since the contour bump model was completely submerged in the boundary layer; the contour bump was subjected to both subsonic and supersonic incoming flow. The subsonic flow region appears in between $0 < y < 7.6$ mm and the supersonic flow region exists in anywhere within the flow field where $y > 7.6$ mm [6].

2.2. Rounded contour bumps

Two rounded, three-dimensional contour bump models, known as the VG bump and the longitudinal jet bump were used in the present experimental study. These two contour bump models have the same general geometry as shown in Fig. 2a (adopted from [6]) but incorporated with different passive flow control devices. The dimensions of these two bump models are 75 mm (length) × 50 mm (width) × 10 mm (apex height). It should be noted that contour bumps with identical general geometry also employed in

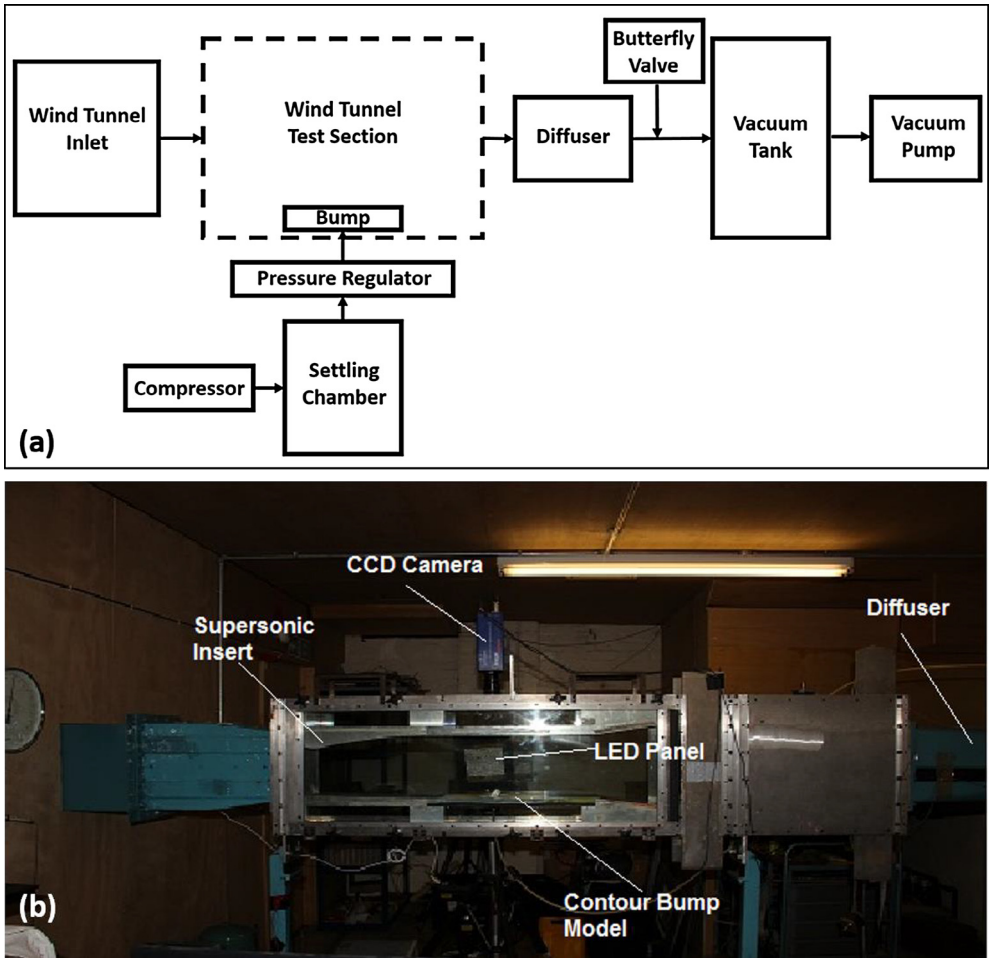

Fig. 1. (a) Systematic diagram of the supersonic wind tunnel facility used (adopted from [6]). (b) Snapshot of the actual supersonic wind tunnel used in the present study.

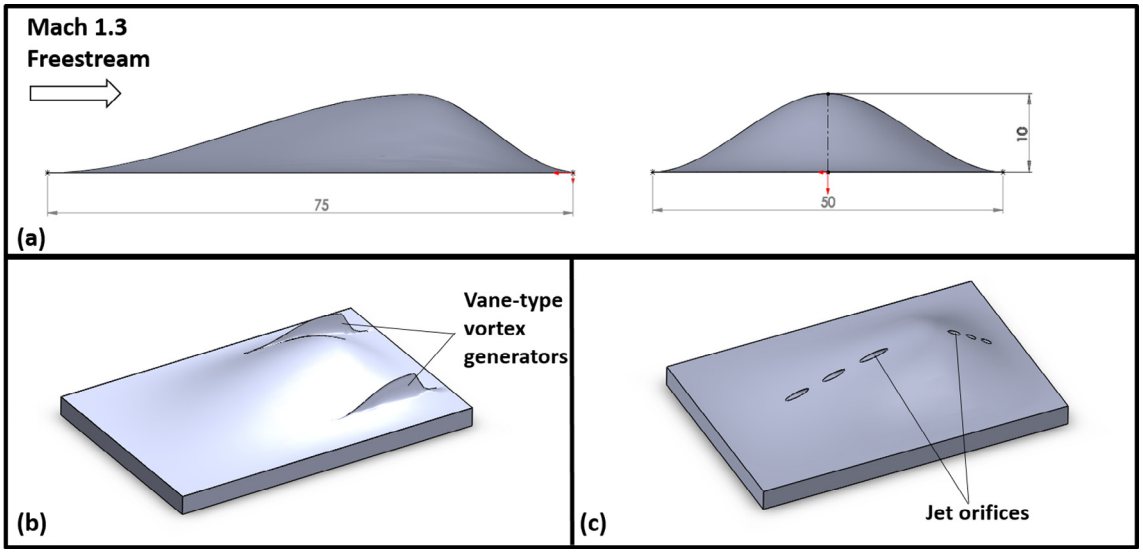

Fig. 2. Schematic diagram of the rounded contour bump. (a) General contour bump geometry (adopted from [6]), (b) VG bump and (c) longitudinal jet bump.

Lo and Kontis [6,8], Lo et al. [7], Qin et al. [12], Wong et al. [13] and Zare-Behtash et al. [23].

In the VG bump, a pair of backward-facing counter-rotating vane-type vortex generators is installed downstream of the bump crest at the two sides of the bump as shown in Fig. 2b. It should be noted that the details geometry, dimensions and locations of this vane-type vortex generator pair is shown in Fig. A1 in Appendix A. The length, apex height and maximum thickness of the two

vanes are 22 mm, 5 mm and 3 mm, respectively. The front of these two vane-type vortex generators are located at 48 mm downstream of the bump front. The centreline-to-centreline distance between the bump and each vane is 14 mm. It is aimed that the streamwise vortices generated by these two vortex generators could enhance flow mixing between the low-energy boundary layer and the freestream in attempt to achieve flow separation control downstream of the bump crest. In the longitudinal jet bump, passive by-pass jet is used to divert some incoming flow upstream of the bump crest to the bump valley in attempt to alter the flow pattern in the wake region. Three 1 mm diameter circular-shaped channels aligned longitudinally along the bump centreline are provided to connect the ramp-shaped front surface with the valley of the longitudinal jet bump. These three channels are located at 3 mm, 5 mm and 7 mm below the bump crest. A schematic of the longitudinal jet bump is displayed in Fig. 2c.

3. Flow diagnostics

3.1. Surface oil flow visualisation

Qualitative spanwise flow pattern over the two rounded contour bumps being studied was resolved using surface oil flow visualisation. The experimental setup used was identical to that shown in [6] and only a brief description is given here. The two rounded contour bump models were first sprayed with five layers of matt black paint prior to the experiments. Three colours of fluorescent dye (i.e. green, red and white) were applied 100 mm upstream of the front of the contour bump model using pipettes so that the effect of flow mixing along the bump could be identified [6,8]. Illumination to the wind tunnel test section was achieved through a pair of UV (Ultra-Violet) LED (Light Emitting Diode) panels with maximum emission wavelength of 395 nm [6–8]. These panels were placed at the two sides of the wind tunnel test section. Wind-on images were captured continuously in the surface oil flow visualisation experiments using a ceiling mounted Canon EOS600D Single Lens Reflection (SLR) camera. The camera has a maximum resolution of 14 mega-pixels and the ISO speed, shutter speed and aperture size were ISO400, 1/4000 s and F11, respectively.

3.2. High-speed monochrome Schlieren photography

Streamwise flow pattern over the contour bump models was visualised using the conventional mono-chrome Topler's z-type high-speed Schlieren photography technique. The setup employed in the present study was identical to that employed in [6–8,24–32]. Illumination to the wind tunnel test section was achieved using a 450 W continuous Xenon arc-lamp. The illuminating light source was first focused by a focusing lens and then passed through a 2 mm wide slit. The expanding light beam was then reflected by the first parabolic mirror to reach the wind tunnel test section followed by the second parabolic mirror. The focal length and diameter of these two parabolic mirrors are 2088 mm and 203.2 mm, respectively. After reflecting from the second parabolic mirror, the light beams passed through a horizontal knife edge and then reaching the Photron FastCam SA1.1 high-speed mono-chrome camera at which the high-speed Schlieren images were recorded. In the high-speed Schlieren photography experiments, the frame rate and resolution of the camera were kept constant at 5000 frames per second and 1024 pixels $\times$ 1024 pixels, respectively. The exposure time was set to 1 μs so that the unsteady effects in the flow field could be captured. Captured images were stored in a Windows-based personal computer and processed using the open-source software Image J.

3.3. Two-component particle image velocimetry measurements

Time-averaged velocity and turbulence level information along the centreline of the contour bump models was obtained using time-averaged two-component Particle Image Velocimetry (PIV) measurements. The setup of the PIV measurement experiments was identical to that employed in [5,6,33–35] and hence, only a brief description is provided here. A Litron Nano L-series, Nd:YAG Model LPU550 Q-switched double-pulsed laser with maximum pulse energy output of 200 mJ was used to provide illumination. The repetition rate, laser pulse wavelength and pulse width are 15 Hz, 532 nm and 4 ns, respectively. A movable guide arm was used to deliver the laser beam to reach the wind tunnel test section. A series of optics was mounted at the end of the laser guide arm so that a thin laser sheet with typical thickness of 0.8 mm was obtained. The laser sheet illuminated along the centreline of the wind tunnel test section. The time delay between the two laser pulses (Δt) was set to $\Delta t = 0.8$ μs which was calculated based on the freestream velocity and the interrogation window size used in the PIV measurements. Through this setting, the seeder particle movement between two consecutive frames was 4 pixels or 0.36 mm. Olive oil particles with typical particle size of 1 μm were used as the seeder particles. The seeder particles were generated using a TSI Model 9307 oil droplet generator and delivered to the inlet of the supersonic wind tunnel through a flexible hose. The corresponding Stokes number (Stk) of the seeder particles is Stk = 0.022 so that the requirement of $Stk \ll 1$ is satisfied. This ensured that the seeder particles could accurately follow the flow streaklines.

A LaVision Imager Pro X 2M CCD (Charge-Coupled Device) camera which viewed the illuminating laser sheet orthogonally was used to capture the scattered light reflected from the seeder particles. The camera has a resolution of 1600 pixels $\times$ 1200 pixels. A Nikon 28–82 mm zoom lens was mounted at the front of the camera so that a viewing area of 143 mm (length) $\times$ 107 mm (height) was obtained. The background noise generated from the area surrounding the wind tunnel test section was removed by a 532 nm narrow band-pass filter which mounted in front of the camera lens. The time-averaged vector fields over the contour bump model were constructed by averaging a minimum of 300 image pairs. The raw images captured from the PIV measurements were stored in a Windows-based workstation and processed using the software Davis 7.2. The recorded images were first divided into a number of 64 pixels $\times$ 64 pixels (i.e. 5.7 mm $\times$ 5.7 mm) interrogation windows and two passes of cross-correlation were conducted. The interrogation window size was then refined to 32 $\times$ 32 pixels and another three passes of cross-correlation were conducted. It should be noted that a 50% overlapping was used between neighbouring interrogation windows in order to increase the accuracy of the vector field that resolved. Uncertainty in the PIV measurements was approximately 6.3% as mentioned in the article recently published by Lo and Kontis [6]. It was calculated using the approach developed by Lusk [36] and later adopted by Lusk et al. [37,38] and Lo et al. [39,40].

4. Results and discussion

4.1. Spanwise flow pattern

Spanwise flow pattern over the VG bump and the longitudinal jet bump is visualised using surface oil flow visualisation and the results obtained are shown in Fig. 3. It should be noted that the spanwise flow pattern over the plain rounded contour bump (hereafter: plain bump) adopted from [6] is also presented in Fig. 3 for the purpose of comparison.

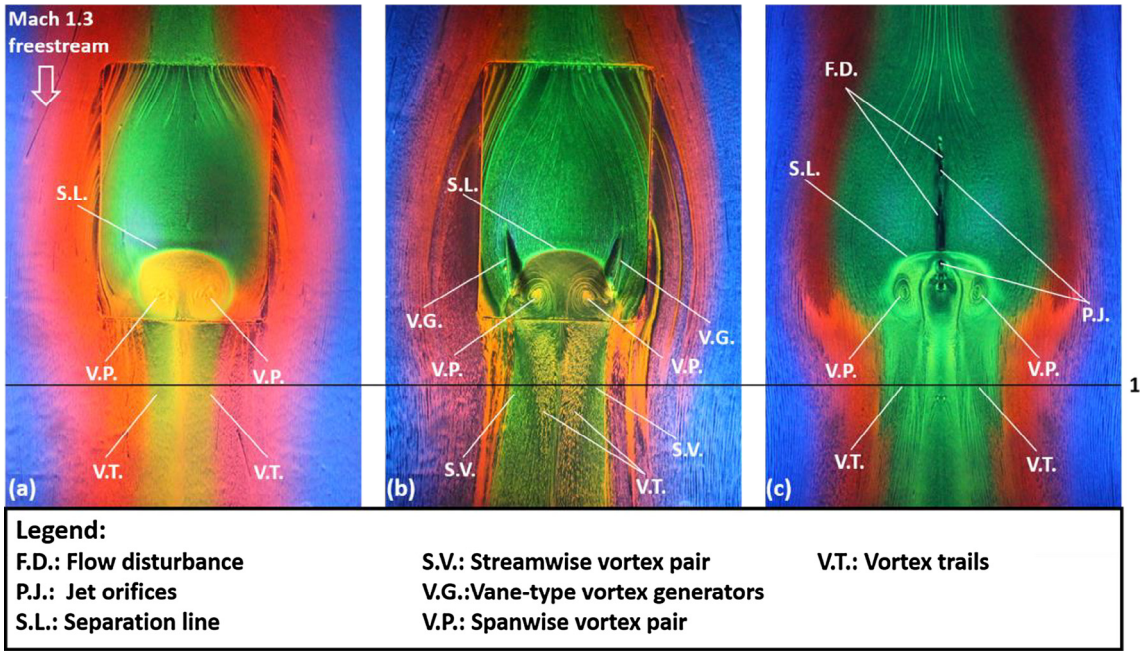

Fig. 3. Spanwise flow pattern over the (a) plain bump (adopted from [6]), (b) VG bump and (c) longitudinal jet bump captured from the surface oil flow visualisation experiment.

The general spanwise flow pattern over the rounded contour bump can be illustrated using the plain bump shown in Fig. 3a. The incoming flow reaching the front of the plain bump is deflected upwards to move along the ramp-shape front face and towards the two sides of the bump. The flow along the bump front surface eventually reaches the bump crest. Since the flow over part of the plain bump is subsonic (i.e. in the region between $0 < y < 7.6$ mm), an adverse pressure gradient is presented in the bump valley. This leads to the occurrence of flow separation at the leeward side of the bump which is evidenced by the presence of a separation line (S.L.) at the bump crest. As a result of the flow separation, a low pressure wake region is formed downstream of the bump crest in the subsonic flow region. This low pressure zone attracts the flow from the two side around the bump to move into and circulate in the bump valley so that a pair of spanwise vortices (V.P.) is formed in the bump valley [6]. This can be observed clearly from Fig. 3a that orange colour oil streaks were left downstream of the bump crest on the surface of the plain bump. This indicates that the formation of the two spanwise vortices in the bump valley is due to flow mixing between the centre portion (i.e. the region that shows green streaklines) and the two sides (i.e. the region that shows red streaklines) of the bump. These two spanwise vortices propagate downstream and hence, two vortex trails (V.T.) are left behind the plain bump.

Fig. 3b, the general spanwise flow pattern upstream of the bump crest is considerably similar to that shown in the plain bump. Downstream of the bump crest, a pair of spanwise vortices (V.P.) is formed in the bump valley resulting from the flow separation that appears in the subsonic flow region downstream of the bump crest. Compared to the two spanwise vortices that shown in the valley of the plain bump (Fig. 3a), the spanwise vortex pair that presents in the VG bump (Fig. 3b) is smaller. In addition, a pair of streamwise horseshoe vortices (S.V.), generated by the two vane-type vortex generators is presented in the bump valley. It is deduced that the presence of this streamwise horseshoe vortex pair locally increases the pressure level in the bump valley so that less flow is attracted to move into the bump valley from the two sides. This might explain why the spanwise vortices that formed in the valley of the VG bumps are smaller than those appeared behind the plain bump. It should be note that the streamwise horseshoe vortex pair (S.V.) shown in Fig. 3b is slightly smeared. Therefore, another image using single colour fluorescent oil that shows the spanwise flow pattern along the VG bump is provided in Appendix B (Fig. B1) for further reference.

Several changes in the spanwise flow pattern can be observed in the longitudinal jet bump (Fig. 3c). Firstly, a small oil-free region (F.D.), caused by the flow disturbance effect due to the presence of the three by-pass jet orifices, occurs in the ramp-shaped front surface of the bump. Similar flow disturbance effect could also be observed when the traverse by-pass jet bump was used as documented in [6]. Downstream of the bump crest of the longitudinal jet bump, the appearance of a separation line (S.L.) indicates the location where flow separation begins. Similar to the plain bump, a pair of spanwise vortices (V.P.) is formed in the bump valley. However, the two spanwise vortices that shown in the bump valley of the longitudinal jet bump (Fig. 3c) are much smaller and more diffuse than those shown in the plain bump (Fig. 3a). In addition, another oil-free region is presented in the bump valley around the centreline of the longitudinal jet bump. It is deduced that the passive by-pass jet that blowing in the bump valley increases the local pressure level around the centre portion of the longitudinal jet bump. Therefore, flow re-circulation is limited to the regions towards the two sides of the bump valley that leads to the formation of smaller and more diffuse spanwise vortices in the bump valley. It should be noted that the three longitudinally-aligned passive by-pass jet orifices at the leeward side of the longitudinally jet bump are not clearly shown compared to those shown at the windward side in Fig. 3c. This is due to the contour bump used has a steeper gradient (relative to the horizontal direction) at the bump valley. As a result, when viewing the longitudinally jet bump from the ceiling of the wind tunnel test section, the three jet orifices at the leeward side seem smaller compared to those at the windward side.

In order to provide a rough account of the effects of the vane-type vortex generators and the longitudinally-aligned passive by-pass jet in affecting the size of the spanwise vortices in the bump

valley, the size (i.e. maximum length and width) of the spanwise vortex pair (V.P.) and the width of the vortex trails (V.T.) in the valley of the plain bump, VG bump and longitudinal jet bump (Fig. 3) were measured and tabulated in Table 1. It should be noted that the width of the two vortex trails (V.T.) was measured 20.5 mm downstream of the rear end of each contour bump, i.e. the horizontal straight line with an index 1 that displayed in Fig. 3.

It is clear from the data presented in Table 1 that both the vane-type vortex generators and the longitudinally aligned passive by-pass jet could reduce the size of the spanwise vortices in the bump valley. For the VG bump, the size of the spanwise vortices and the width of the vortex trails are 2.5% and 3.8% smaller than those shown in the baseline plain bump, respectively. Similarly, the size of the spanwise vortex pair and the width of the vortex trails in the longitudinal jet bump are 4.3% and 29.5% smaller than those presented in the plain bump, respectively. Although the results shown in Table 1 seem to indicate that the use of longitudinally aligned passive by-pass jet could achieve higher effectiveness in wake flow control on rounded control bumps in supersonic freestream, it must be emphasised that these data could only be understood qualitatively. This is because high levels of uncertainty arise when length and width are measured directly from the images obtained from the surface oil flow visualisation experiments.

4.2. Streamwise flow pattern

Qualitative streamwise flow pattern over the VG bump and the longitudinal jet bump is presented in Fig. 4 in the form of Schlieren photography images. It should be noted that the Schlieren image of the plain bump adopted from [6] is also displayed in Fig. 4 for reference purpose. The general streamwise flow pattern over the rounded contour bump could be illustrated using the Schlieren photography image for the plain bump (Fig. 4a). When the incoming flow reaches the beginning of the bump, the flow is deflected to move upwards. As a result, a or a series of compression wave(s) (C.W.) appears at the front of the plain bump. Across the compression wave, the flow moves along the ramp-shaped front surface to reach the bump crest. Flow expansion appears around the bump crest which is evidenced by the presence of a series of expansion waves (E.W.) around that region. This continuous flow expansion leads to the occurrence of a favourable pressure gradient around the bump crest. Downstream of the bump crest, since the flow over part of the bump valley is subsonic, an adverse pressure gradient exists along the concave-shaped bump valley. This results in the appearance of flow separation which is confirmed by the presence of a shear layer (S.L.) downstream of the bump crest. Finally, at the rear end of the bump, another oblique shock wave called the re-attachment shock (R.S.) appears. Across the re-attachment shock the flow becomes parallel to the traverse direction.

It should be noted that there are several weak shock waves (W.S.) emanating from the ceiling of the wind tunnel test section that could be seen in Fig. 4. These weak shock waves are generated by the small gaps that present between the window frame and the top window of the supersonic wind tunnel. Several measures have been made in attempt to reduce the effects caused by these small gaps although they could not be completely sealed. As the strength of these weak wall shock waves is considerably weak; it is believed that the general streamwise flow pattern over the bump models being studied is not significantly affected by the presence of these weak shock waves. The streamwise flow pattern over the VG bump (Fig. 4b) and the longitudinal jet bump is nearly identical to that shown over the plain bump (Fig. 4a). This indicates that the presence of the vane-type vortex generators and the use of longitudinal passive by-pass jet do not induce any observable changes in the streamwise flow pattern over the bump.

Table 1
Size of the spanwise vortex pair and vortex trails measured in the wake region of the plain bump, VG bump and longitudinal jet bump.

	Max. length of the spanwise vortex (mm)	Max. width of the spanwise vortex (mm)	Width of the vortex trails at Point 1 (mm)
Plain bump	14.2	12.2	7.8
VG bump	14.2	11.9	7.5
Longitudinal jet bump	10.4	9.5	5.5

4.3. Velocity and turbulence level information

Time-averaged velocity and turbulence level information along the centreline of the VG and the longitudinal jet bumps is presented in this subsection. It should be noted that the velocity data for the plain bump (adopted from [6]) are provided for the purpose of comparison and to facilitate discussion. The streamlines and the velocity magnitude contours over the plain bump, the VG bump and the longitudinal bump are displayed in Fig. 5. Normalised x- and y-coordinates (x/H and y/H) are used in the data present in this subsection where H is the apex height of the contour bump.

In the plain bump (Fig. 5a), the normalised velocity magnitude contour shows that flow expansion appears in the freestream around and downstream of the bump crest. This means that a favourable pressure gradient is presented. Since the plain bump is submerged in the boundary layer and part of the incoming flow is subsonic; an adverse pressure gradient exists downstream of the bump crest (i.e. the region between $6.5 < x/H < 9.5$ and $0 < y/H < 0.76$). This leads to the occurrence of flow separation which results in the formation of a wake region in the bump valley. From Fig. 5a, it can be seen that the wake region that presents downstream of the bump crest of the plain bump is considerably strong. Similar flow pattern also shown in the VG bump (Fig. 5b) but the wake that presents is slightly longer and its strength is considerably weaker than that occurs in the plain bump. The streamtraces shown over the VG bump (Fig. 5b) indicate that a small vortex appears immediately downstream of the two vane-type vortex generators. It is believed that the two vane-type vortex generators that present generate this small vortex. In the longitudinal jet bump (Fig. 5c), a long and wide wake region is presented behind the bump crest. Its strength is considerably weaker than the wake that formed at the leeward side of the plain bump. In addition, from the streamtraces shown in Fig. 5c, a vortex is formed immediately downstream of the bump crest in the bump valley. The formation of this vortex is due to the presence of an additional longitudinal pressure gradient due to the blowing of the longitudinally aligned passive by-pass jet in the bump valley.

The time-averaged normalised x- and y-velocity contours over the plain bump, the VG bump and the longitudinal jet bump are presented in Fig. 6.

Fig. 6a shows the normalised x- and y-velocity contours of the plain bump. At the front of the plain bump, no obvious x-velocity reduction can be observed in the normalised x-velocity contour. This indicates that the compression waves that present at the beginning of the bump as shown in the Schlieren image (Fig. 4a) are weak. A region that shows high levels of normalised y-velocity appear along the ramp-shaped front surface of the plain bump which means the flow moves forwards and upwards at that region. Flow expansion occurs around the bump crest which is evidenced by the significant increase in the normalised x-velocity around that region. Downstream of the bump crest in the freestream, the flow moves forwards and downwards which can be confirmed by observing the normalised y-velocity contour that negative normalised y-velocity occurs around and downstream of

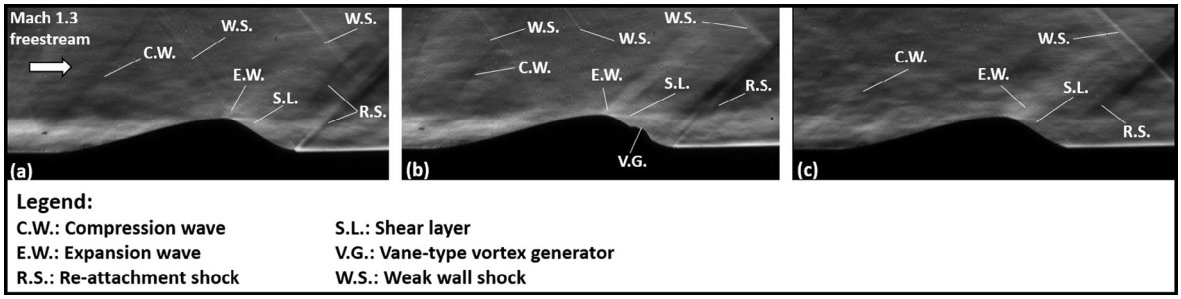

Fig. 4. Schlieren photography images of the (a) plain bump (adopted from [6]), (b) VG bump and (c) longitudinal jet bump.

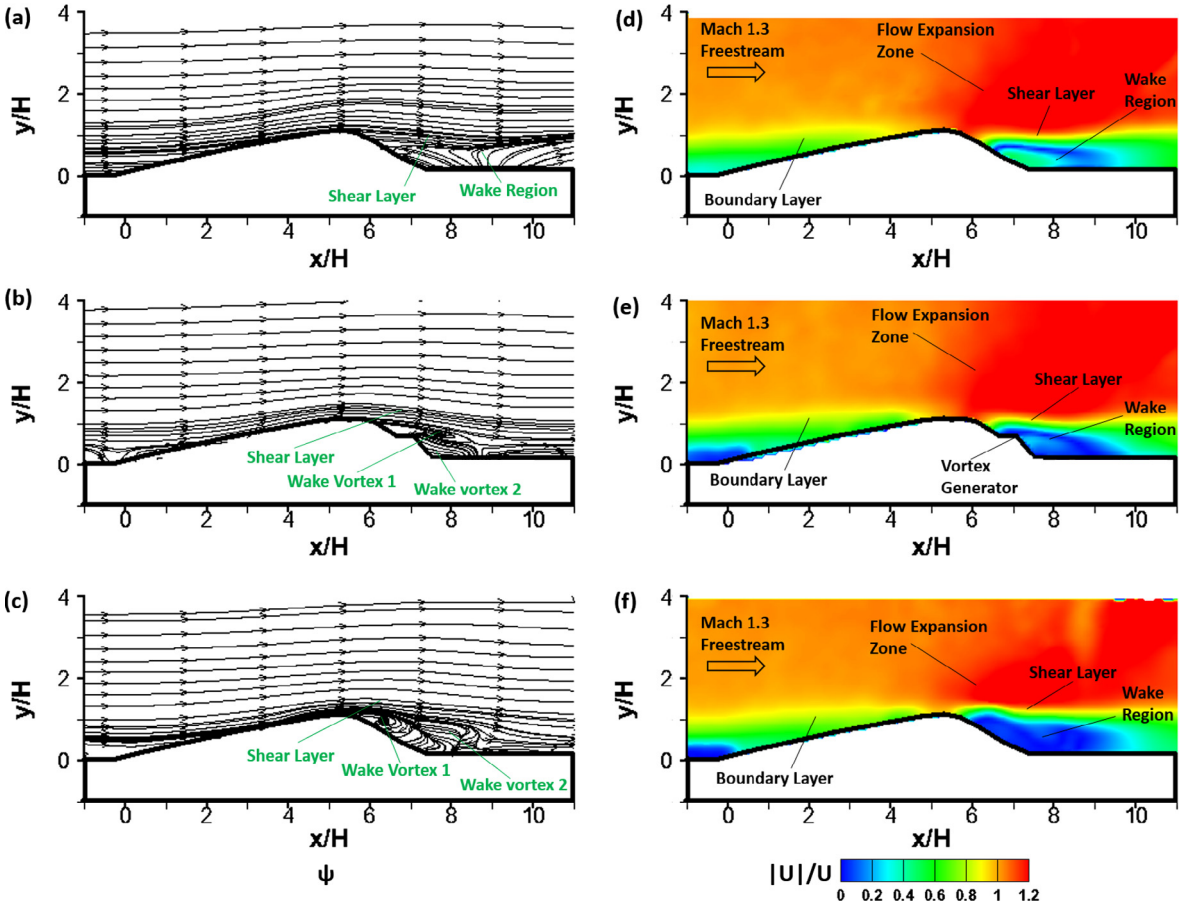

Fig. 5. Flow streamlines and the normalised velocity magnitude contours over the centreline of the (a) plain bump (adopted from [6]), (b) VG bump and (c) longitudinal jet bump.

the bump crest of the plain bump. Downstream of the bump crest, in the subsonic flow region (i.e. the region between $0 < y/H < 0.76$), a wake region featured with reverse flow is presented at the leeward side of the plain bump. The size of this wake region is about $0.27\,c \times 0.093\,c$ (length × height) where c is the bump length which is 75 mm. This indicates that the length and height of the wake region of the plain bump are approximately 36% and 12% of the bump length, respectively.

In the VG bump (Fig. 6b), the normalised x- and y-velocity contours that present are similar to those shown in the plain bump. A slight difference can be observed in the bump valley when the normalised x-velocity contour of the VG bump is compared with that of the plain bump. Qualitatively, from Fig. 6b, the wake region of the VG bump is slightly longer and taller than that of the plain bump. In fact, its size is about 0.38 c and 0.1 c which means that the length and height of the wake region of the VG bump are 51% and 13% of the bump length, respectively. This means that the presence of the two vane-type vortex generators at the two sides of the VG bump could not reduce the size of the wake region. In contrast, they increase the length and height of the wake region that present. It is interesting to note that as seen in the normalised y-velocity contour of the VG bump (Fig. 6b), the region that shows flow expansion around the bump crest is longer and stronger than that present in the plain bump. This might explain why a longer reverse flow region exists at the leeward side of the VG bump.

Some interesting changes occur in the wake region of the longitudinal jet bump. From the normalised x-velocity contour shown in Fig. 6c, it can be seen that the size of the wake region of the longitudinal jet bump is about $0.36\,c \times 0.1\,c$ which is comparable to that shown in the VG bump. This finding implies that the

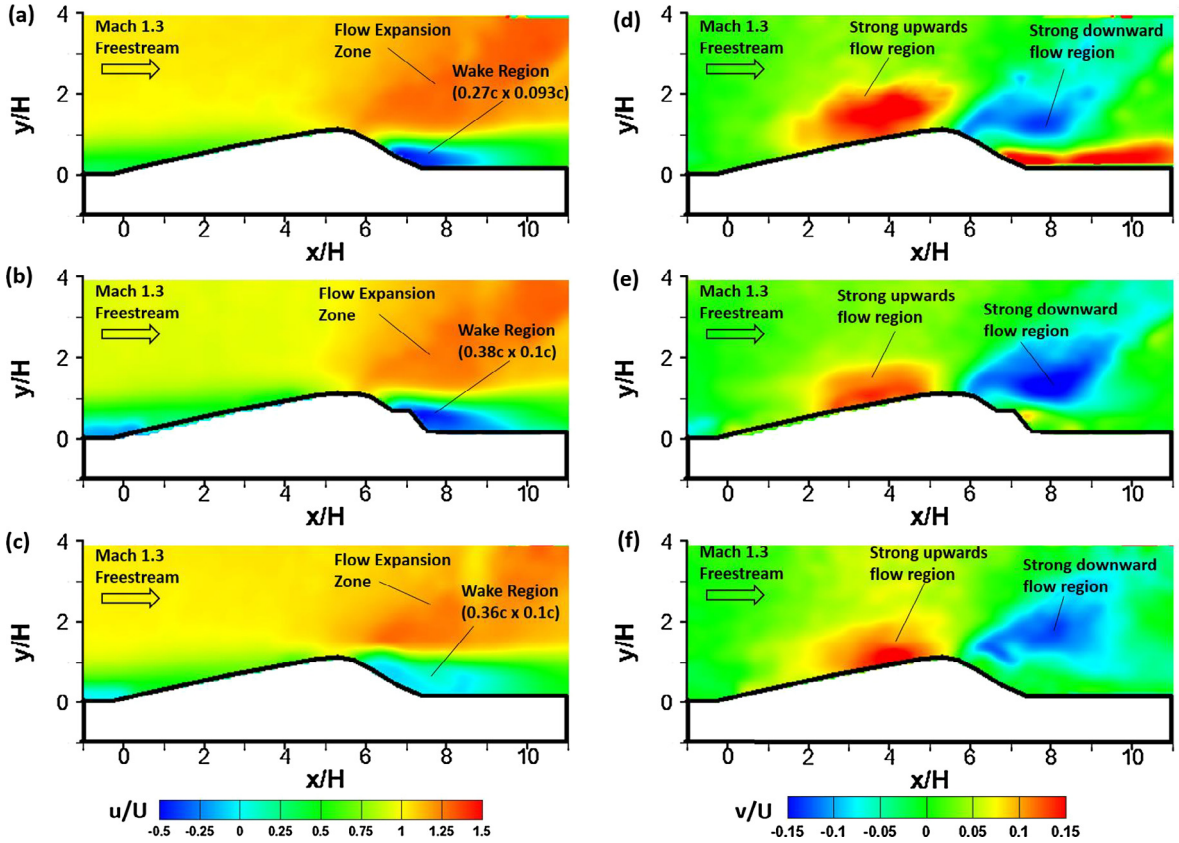

Fig. 6. Normalised velocity contours along the x- and y-directions over the centreline of the (a) plain bump (adopted from [6]), (b) VG bump and (c) longitudinal jet bump.

longitudinally aligned passive by-pass jet that blowing in the bump valley could not reduce the size of the wake region that formed. However, it is observed that the strength of the wake region is considerably weaker than that shown in both the plain bump and the VG bump. This is evidenced that higher flow velocity in x-direction exists along the wake region of the longitudinal jet bump than that of the plain bump and the VG bump. Qualitatively, from the normalised x-velocity contour (Fig. 6c), it can be seen that nearly no negative x-velocity is presented in the wake region of the longitudinal jet bump. This deduces that the longitudinally aligned passive by-pass jet that blowing in the bump valley increases the momentum of the flow in the wake region. This in-turn means that the flow in the wake region of the longitudinal jet bump has higher capability to resist the occurrence of reverse flow than that in the plain bump and the VG bump. The normalised y-velocity contour of the longitudinal jet bump is comparable to that shown in the plain bump although the flow expansion region around the bump crest of the longitudinal jet bump is shorter than that present in the VG bump.

Flow characteristics downstream of the bump crest of the VG bump and the longitudinal jet bump can be further quantified by considering the x- and y-velocity profiles along the wake region as shown in Figs. 7 and 8, respectively. Also, the x- and y-velocity profiles along the wake region of the plain bump are provided in Figs. 7 and 8 for the purpose of comparison.

It is clear that at the normalised x-location x/H = 6 (Fig. 7a), no reverse flow appears in the wake region of all the three contour bumps being studied. The flow velocity in the wake region returns to the freestream velocity at y/H = 0.75, 1 and 1.3 for the plain bump, the VG bump and the longitudinal jet bump, respectively. At the normalised x-location x/H = 7 (Fig. 7b), reverse flow appears in all of the three bumps being studied. Strongest reverse flow occurs in the wake region of the plain bump at x/H = 7 with its magnitude equals to approximately $u/U_\infty = -0.5$. Similarly, reverse flow also exists at that location in the longitudinal jet bump with its magnitude equal to around $u/U_\infty = -0.05$. This suggests that blowing longitudinally aligned passive by-pass jet could increase the momentum of the flow to resist the occurrence of flow reversal in the wake region of the longitudinal jet bump.

At the normalised x-location x/H = 8 (Fig. 7c), reverse flow only appears in the wake region of the plain bump and the VG bump. However, the strength of the reverse flow is weaker in the VG bump than that of the plain bump. This deduces that the streamwise vortices that generated by the two vane-type vortex generators in the VG bump increases the flow momentum of the flow in the wake region of the VG bump from that normalised x-location onwards. No reverse flow is shown in the wake region of the longitudinal jet bump from x/H = 7 onwards. This further confirms that the blowing passive by-pass jet in the bump valley could increase the momentum of the flow in the wake region to increase its capability to resist the occurrence of flow reversal. At the normalised x-location x/H = 9 (Fig. 7d), only forward moving flow is presented in all of the bump being studied. The normalised x-velocity in the longitudinal jet bump at the normalised y-location $0.2 < y/H < 0.5$ is slightly higher than that shown in both the plain bump and the VG bump. The data shown in Fig. 7 proposed that the use of the vane-type vortex generators and longitudinally aligned passive by-pass jet could not reduce the size but instead shows some positive effects in reducing the strength of the wake region at the leeward side of rounded contour bumps.

For the normalised y-velocity profiles measured downstream of the bump crest, from Fig. 8, it can be seen that negative normalised y-velocity (i.e. downwards flow movement) exists in all the normalised x-locations being studied. From the normalised

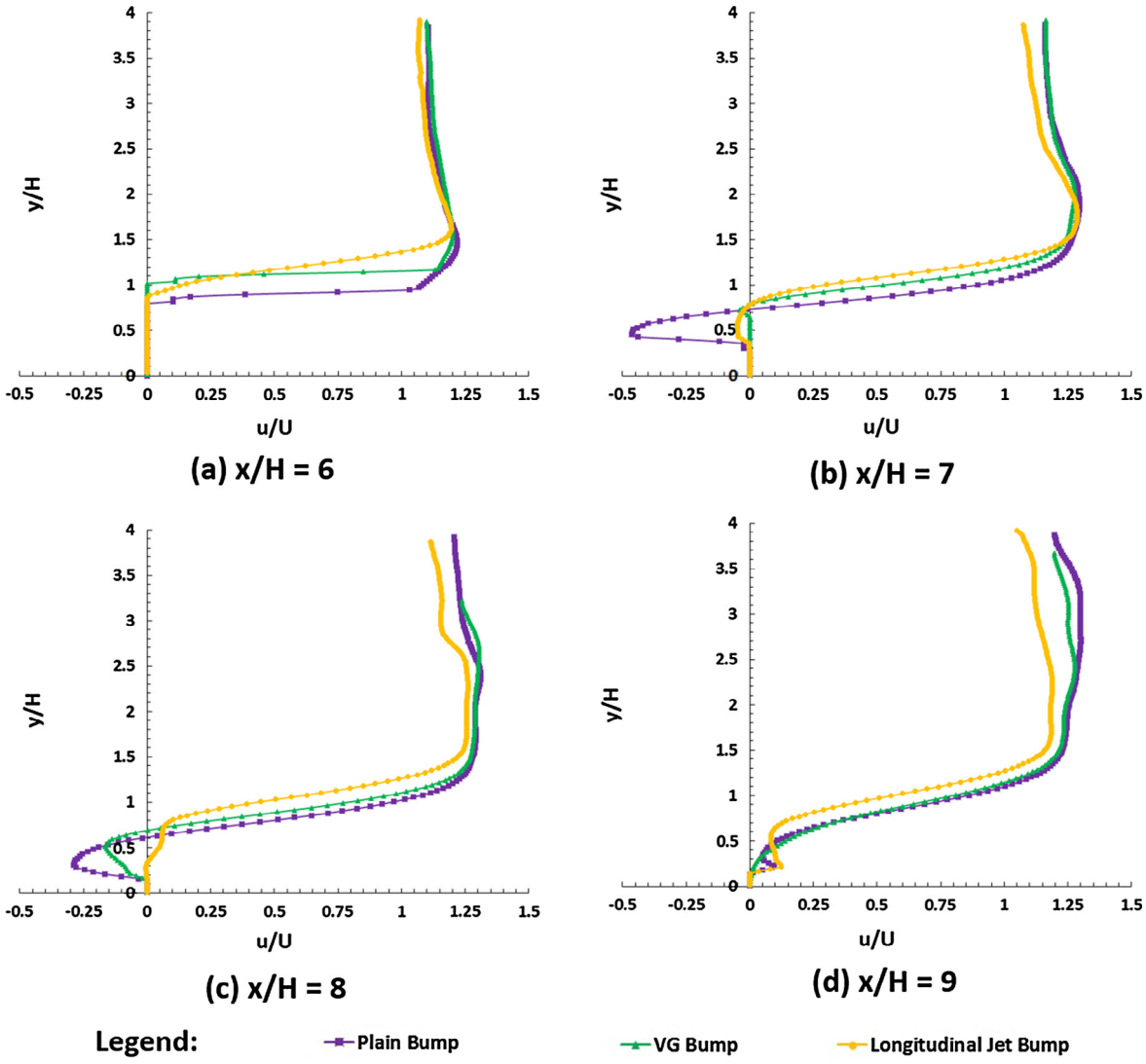

Fig. 7. Normalised velocity profiles in x-direction along the wake region of the (a) plain bump, (b) VG bump and (c) longitudinal jet bump.

x-location x/H = 7 onwards, strongest downwards flow appears in the VG bump followed by the longitudinal jet bump. The weakest downwards flow occurs at the leeward side of the plain bump. In contrast, in the boundary layer (i.e. the region between $0 < y/H < 1.5$), strongest positive normalised y-velocity appears in the wake region of the plain bump at the normalised x-locations $7 < x/H < 9$. This indicates that strong upward flow movement is presented along the wake region of the plain bump. In contrast, considerably weak normalised y-velocity (i.e. relatively weak vertical flow movement) exists along the wake region of both the VG bump and the longitudinal jet bump.

The flow turbulence properties along the wake region of the VG bump and the longitudinal jet bump can be quantified by considering the rms (root-mean-square) x- and y-velocity profiles as shown in Figs. 9 and 10, respectively. The rms x- and y-velocity information along the wake region of the plain bump is also given in Figs. 9 and 10 for the purpose of comparison. At the normalised x-location x/H = 6 (Fig. 9a), the longitudinal jet bump possesses high levels of normalised rms x-velocity in the shear layer (i.e. the region between $0.8 < y/H < 1.7$). This means that the flow in the shear layer is highly turbulent in x-direction at that normalised x-location. This is probably due to the presence of the small vortex at that region as seen in the streamtraces of the longitudinal jet bump shown in Fig. 5c. The rms x-velocity levels at the same region (i.e. $0.8 < y/H < 1.7$ at x/H = 6) for the plain bump and the VG bump are relatively low as no vortical structures are presented in these bumps. At the normalised x-location x/H = 7 (Fig. 9b), in the region between $0.6 < y/H < 1.3$ (i.e. part of the wake and the shear layer), the VG bump shows the highest normalised x-velocity levels amongst the other two bumps being studied. This is due to the presence of a small vortex at that region as shown in the streamtraces of the VG bump (Fig. 5b). In addition, the streamwise vortices that generated by the two vane-type vortex generators also increase the flow turbulence level in x-direction at that region. It is interesting to note that at the normalised x-location x/H = 7, the longitudinal jet bump has the lowest normalised rms x-velocity amongst the three bumps being studied in the region between $0.6 < y/H < 1.3$. This indicates that the blowing by-pass jet in the bump valley could provide flow stabilisation effects from the normalised x-location x/H = 7 onwards.

Similar results shown at the normalised x-location x/H = 7 also appear at the normalised x-locations x/H = 8 and 9 (Fig. 9c and d). At the normalised x-location x/H = 8 and 9, highest levels of normalised rms x-velocity occur in the VG bump amongst the three bumps being studied in the region between $0.2 < y/H < 1.3$ and $0.1 < y/H < 1.4$ (i.e. the wake region and the shear layer), respec-

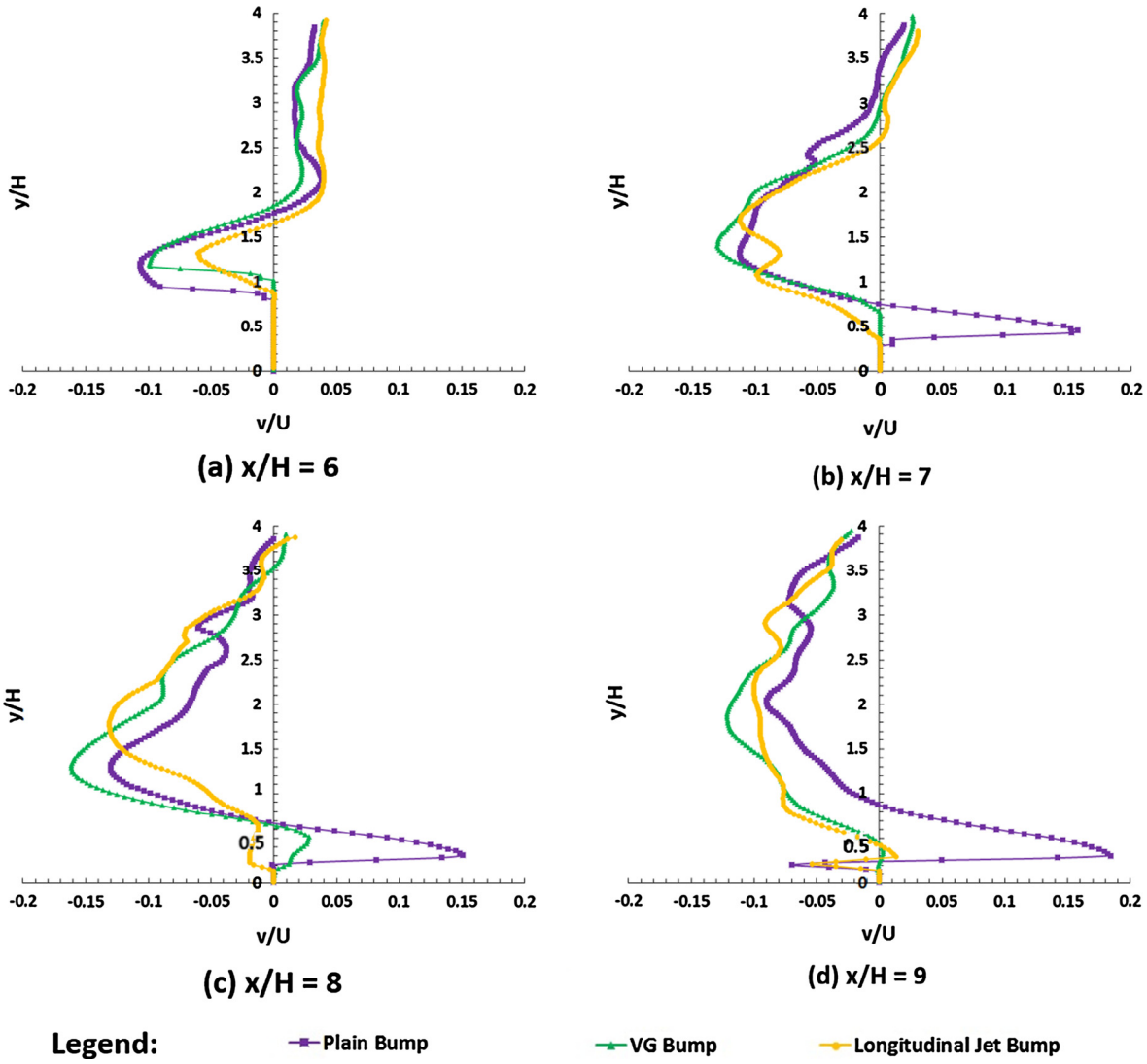

Fig. 8. Normalised velocity profiles in y-direction along the wake region of the (a) plain bump, (b) VG bump and (c) longitudinal jet bump.

tively. This indicates that the size of the region that shows high normalised rms x-velocity and strength of the flow turbulence levels in x-direction increases progressive downstream of the bump crest of the VG bump. This is because the progressively growth in the size and strength of the two streamwise horseshoe vortices generated by the two vane-type vortex generators progressively increase the size and strength of the turbulent flow region along the wake region of the VG bump. In fact, the results obtained in these two normalised x-locations for the VG bump confirmed that the presence of the vane-type vortex generators in the VG bump could enhance flow mixing between the low-energy boundary layer and the freestream (thus increasing the flow turbulence level) which leads to the reduction in the strength of the wake region. In contrast, in the plain bump and the longitudinal jet bump, the normalised rms x-velocity levels in the region between $0.6 < y/H < 1.3$ decrease progressive from the normalised locations $x/H = 8$–9. At these two normalised x-locations, the normalised rms x-velocity levels of the longitudinal jet bump are slightly lower than those shown in the plain bump at the same region. This further implies that the blowing longitudinally aligned passive by-pass jet in the bump valley could provide flow stabilisation effects along the wake region.

In the normalised rms y-velocity profiles, similar normalised y-velocity profiles appear in all of the three contour bumps being studied at the normalised x-location $x/H = 6$ (Fig. 10a). At the normalised x-location $x/H = 7$ (Fig. 10b), amongst the three bumps being studied, the plain bump possesses the highest normalised rms y-velocity levels in the region between $0.3 < y/H < 0.8$, (i.e. the wake region) while the VG bump has the lowest normalised rms y-velocity levels at the same region. The trends of normalised y-velocity levels that shown in the normalised x-locations $x/H = 8$ (Fig. 10c) and $x/H = 9$ (Fig. 10d) are similar to those displayed in the normalised rms x-velocity profiles shown in Fig. 9. The VG bump has the highest normalised rms y-velocity levels in the region between $0.2 < y/H < 1.3$ (i.e. the wake region and the shear layer) at these two normalised x-locations due to the flow mixing effects induced by the two streamwise horseshoe vortices that present. Similarly, amongst the three bumps being studied, the longitudinal jet bump shows the lowest normalised rms y-velocity levels in the wake region and the shear layer (i.e. the region between $0.2 < y/H < 1.3$) at the normalised x-locations $x/H = 8$ and 9. This further confirms that blowing longitudinally aligned passive by-pass jet could provide flow stabilisation effects along the wake region.

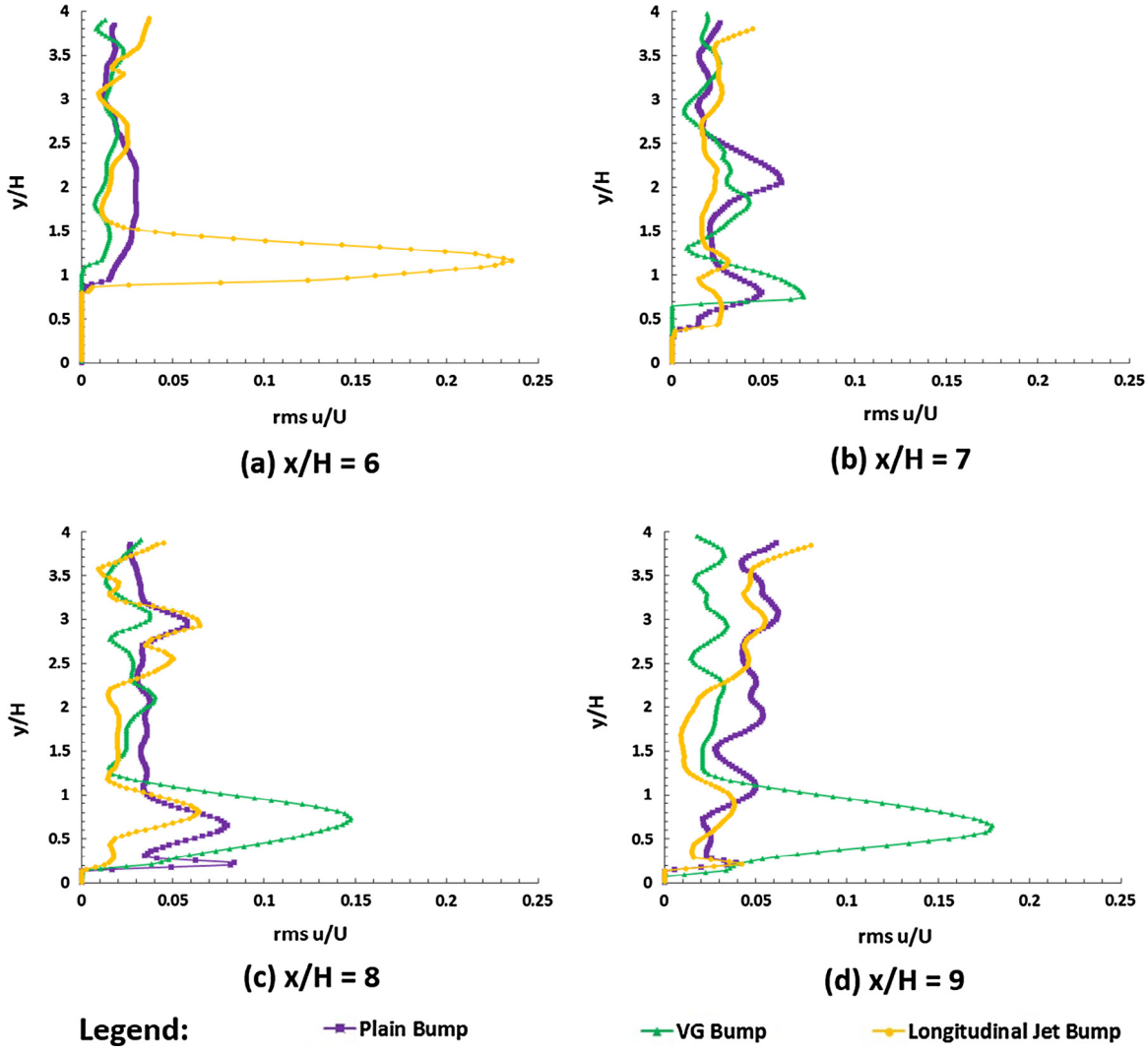

Fig. 9. Normalised rms x-velocity profiles along the wake region of the (a) plain bump, (b) VG bump and (c) longitudinal jet bump.

The turbulence levels along the wake region of the plain bump, VG bump and longitudinal jet bump could be further quantified by considering their normalised turbulence kinetic energy profiles (tke/U^2) at the normalised x-locations $6 < x/H < 9$ shown in Fig. 11.

It can be seen from Fig. 11 that in the longitudinally jet bump, high levels of turbulence kinetic energy appear at the normalised x-location $x/H = 6$ (Fig. 11a) in the region between $0.95 < y/H < 1.5$. Downstream of $x/H = 6$ the turbulence kinetic energy levels that appear along the wake region (i.e. $0.2 < y/H < 1$) of the longitudinally jet bump are generally lowered than those shown along the wake region of the plain bump (Fig. 11b–d). This further confirms that blowing longitudinally passive by-pass jet in the bump valley could reduce the turbulence levels of the flow and provide flow stabilisation effect along the wake region of the bump. Similar flow stabilisation effects were also observed in Chen et al. [16,17] using passive jet blowing at the leeward side of a stationary circular cylinder in a subsonic freestream. In contrast, from Fig. 11, it can be seen that the turbulence kinetic energy levels along the wake region of the VG bump are considerably higher than those shown along the wake region of the plain bump. This is expected due to the presence of the two vane-type vortex generators on the VG bump induce flow mixing downstream of the bump crest. As a result, high levels of turbulence kinetic energy are observed along the wake region of the VG bump.

The normalised Reynolds stress profiles in the xy-plane along the wake region of the plain bump, the VG bump and the longitudinal jet bump are displayed in Fig. 12.

At the normalised x-location $x/H = 6$ (Fig. 12a), low levels of normalised Reynolds stress in the xy-plane appear in the plain bump and the VG bump. Amongst the three bumps being studied, relatively high levels (in both positive and negative directions) of normalised Reynolds stress in the xy-plane exist in the region between $0.8 < y/H < 1.3$ in the longitudinal jet bump. This is due to the presence of the small vortex at that normalised x-location as shown in the streamtraces (Fig. 5c). At $x/H = 7$ (Fig. 12b), the longitudinal jet bump shows the lowest levels of normalised Reynolds stress in the xy-plane along the entire normalised y-plane being studied. This is due to the flow stabilisation effects provided by the longitudinally aligned passive by-pass jet that blowing in the bump valley. The plain bump and the VG bump show similar levels of the normalised Reynolds stress in the xy-plane in the region between $0.5 < y/H < 1$ at the normalised x-location $x/H = 7$.

Highest normalised Reynolds stress in the xy-plane is shown in the VG bump in the region between $0.2 < y/H < 1.3$ at the normalised x-location $x/H = 8$ (Fig. 12c). Similar to the conclusion drawn when discussing the rms x- and y-velocity levels previously; the presence of the two streamwise horseshoe vortices generated by the two vane-type vortex generators in the VG bump

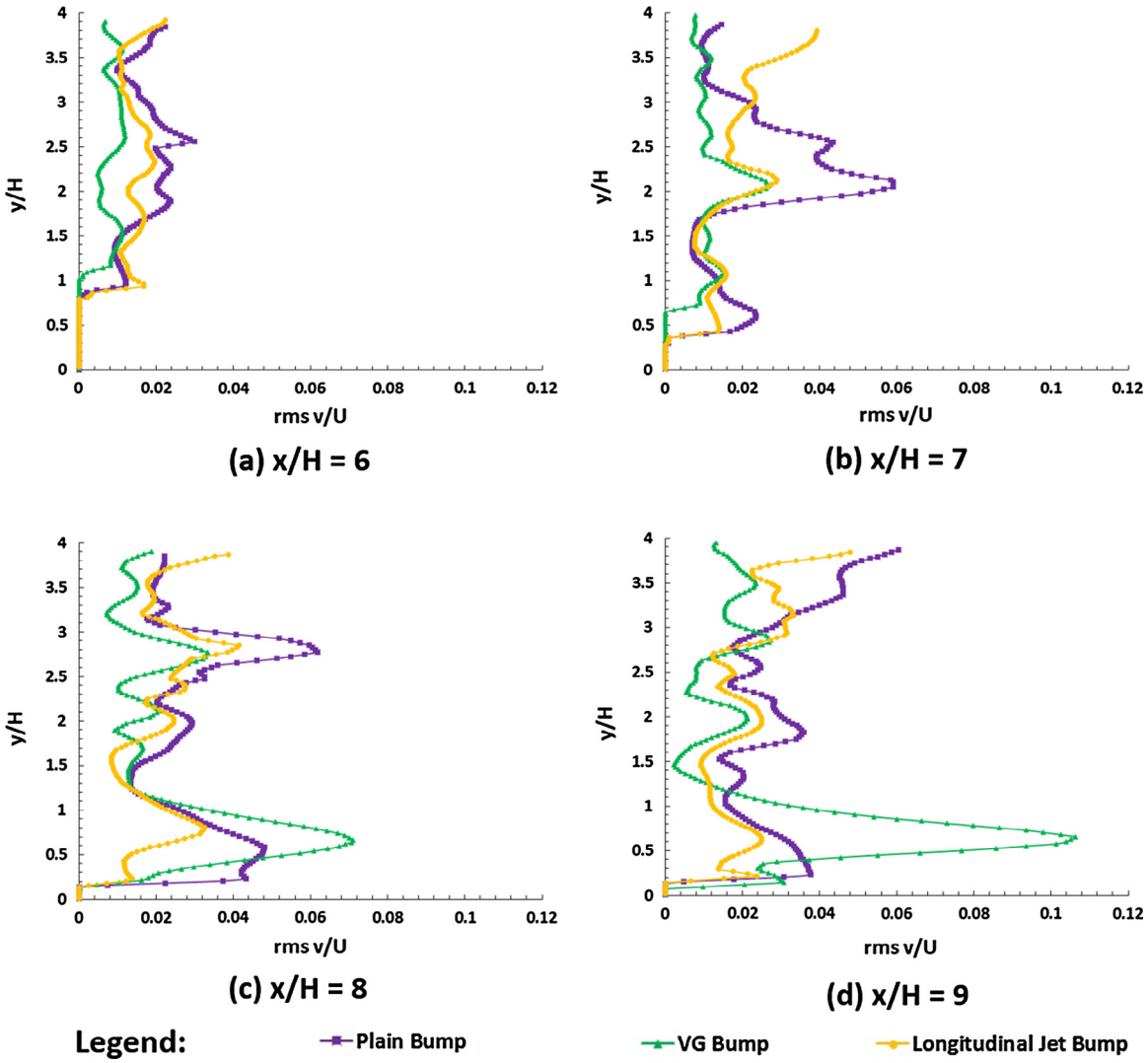

Fig. 10. Normalised rms y-velocity profiles along the wake region of the (a) plain bump, (b) VG bump and (c) longitudinal jet bump.

enhances flow mixing between the flow in the wake region and the freestream. As a result, high levels of normalised Reynolds stress in the xy-plane occur in the wake region and the shear layer of the VG bump. The longitudinal jet bump possesses the lowest levels of normalised Reynolds stress in the xy-plane in the wake region and the shear layer amongst the three bumps being studied. This is due to the flow stabilisation effects provided by the blowing longitudinally aligned passive jet in the bump valley.

Finally, at the normalised x-location x/H = 9 (Fig. 12d), the VG bump still possesses the highest levels of normalised Reynolds stress in the xy-plane in the wake region and the shear layer (i.e. $0.2 < y/H < 1.3$). In fact, its levels at this normalised x-location increase significantly from the normalised Reynolds stress levels that shown at the location x/H = 8. This is because the two streamwise horseshoe vortices generated by the two vane-type vortex generators in the VG bump grow progressively in terms of both the size and strength when they propagate downstream along the wake region. This further confirms that the presence of these two streamwise horseshoe vortices could enhance flow mixing along the wake region of the VG bump. In the plain bump and the longitudinal jet bump, at the normalised x-location x/H = 9 (Fig. 12d), low levels of normalised Reynolds stress in the xy-plane exist in the wake region and the shear layer (i.e. $0.2 < y/H < 1.3$) of these bumps. This finding further suggests that the use of longitudinally aligned passive by-pass jet could provide flow stabilisation effects in the wake region.

5. Limitations of study and future research recommendation

As with other experimental studies, the present study possesses several limitations. Firstly, PIV measurements were only conducted along the centreline of the contour bump being studied. As a result, the flow pattern along other planes are unclear. Further measurements using PIV in other planes are recommended to be conducted in order to fully understand the effects of the vane-type vortex generators and the longitudinally aligned passive by-pass jet in achieving flow control in contour bumps. Secondly, no drag values could be extracted from the PIV data to estimate the flow control effectiveness of both the vane-type vortex generators and longitudinally aligned passive by-pass jet. This is because in order to estimate the drag value over a three-dimensional object, volumetric-PIV measurements would be required to conduct. In order to assess the flow control effectiveness of these two passive flow control methods in rounded contour bumps in supersonic freestream, it is recommended that force balance measurements to be conducted

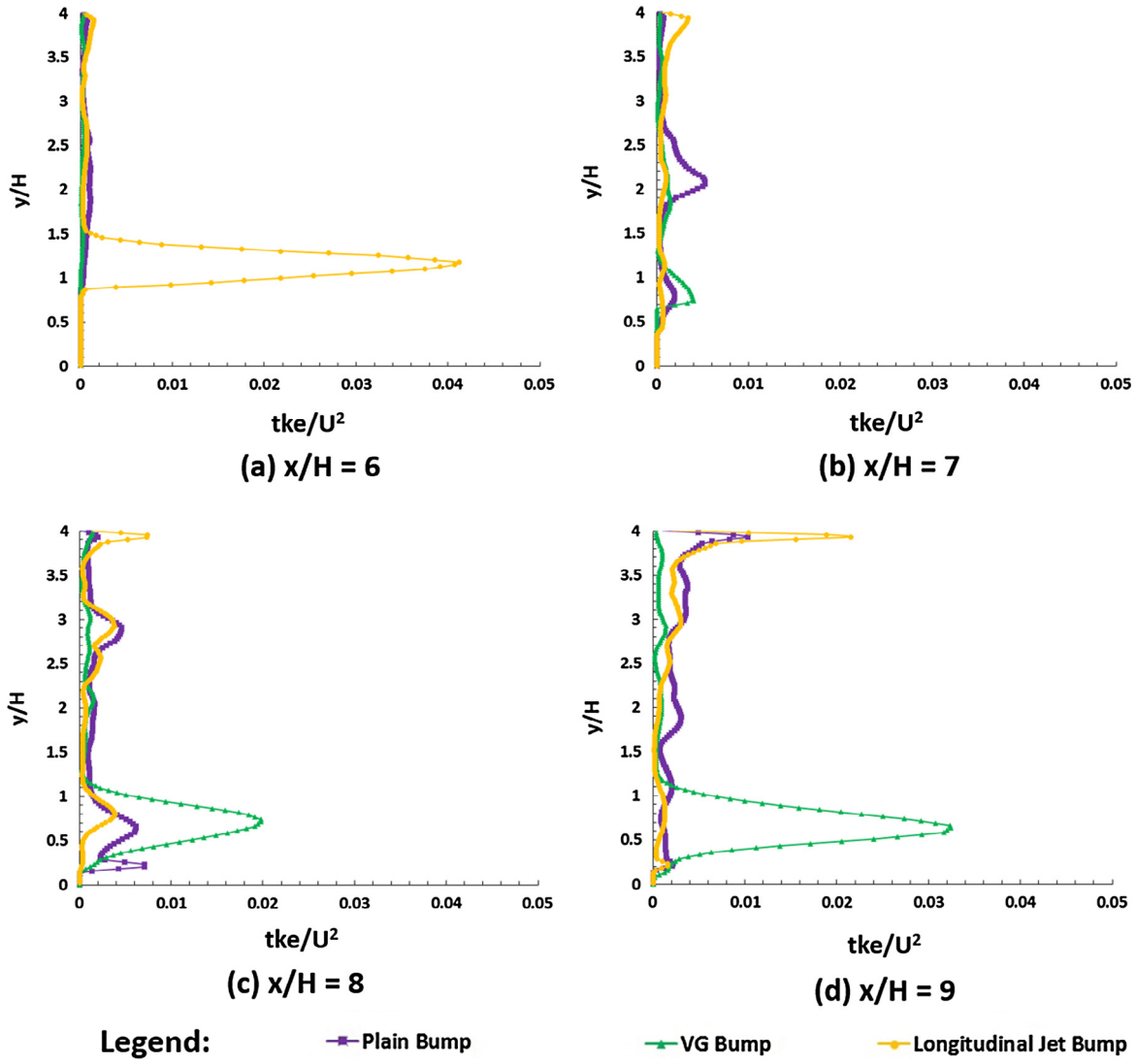

Fig. 11. Normalised turbulence kinetic energy profiles along the wake region of the (a) plain bump, (b) VG bump and (c) longitudinal jet bump.

so that the aerodynamic forces that act on a contour bump with and without various flow control strategies implemented could be measured. Finally, pressure measurements were not included in the present study. This is because incorporating conventional pressure taps in rounded contour bumps would damage the bump surface and would disturb the flow pattern over the entire bump. Therefore, it is recommended that some non-intrusive methods such as pressure-sensitive paint measurements should be used to measure the surface pressure distribution over the entire contour bump model.

6. Conclusions

An experimental study has been conducted to investigate the flow characteristics over the VG bump and the longitudinal jet bump. Surface oil flow visualisation, high-speed Schlieren photography and time-averaged two-component particle image velocimetry were used for flow diagnostics. Results collected from the surface oil flow visualisation experiments indicate that a pair of streamwise horseshoe vortices is generated by the two vane-type vortex generators that present in the VG bump. In addition, a pair of spanwise vortices is formed in the valley of the VG bump and these vortices are smaller than those shown in the plain bump. The spanwise vortices that formed in the valley of the longitudinal jet bump also smaller than those present in the plain bump and their vortex cores are more diffuse. It is deduced that the longitudinally aligned passive by-pass jet that blowing in the bump valley hinders the formation and distorts the vortex core of the spanwise vortices in the bump valley. The results obtained from the high-speed Schlieren photography experiments show that very similar streamwise flow pattern appears in all of the three three-dimensional rounded contour bumps being studied.

Based on the data collected from the time-averaged two-component particle image velocimetry measurements, it was found that the use of both the vane-type vortex generators and longitudinally aligned passive by-pass jet could not reduce the size of the wake region. However, these flow control devices could reduce the strength of the wake region that formed at the leeward side of the bumps. It was deduced that in the VG bump, the two streamwise horseshoe vortices that generated by the vane-type vortex generators enhance flow mixing between the flow in the wake region and the freestream. This in-turn increases the momentum of the flow in the wake region. The effect of flow

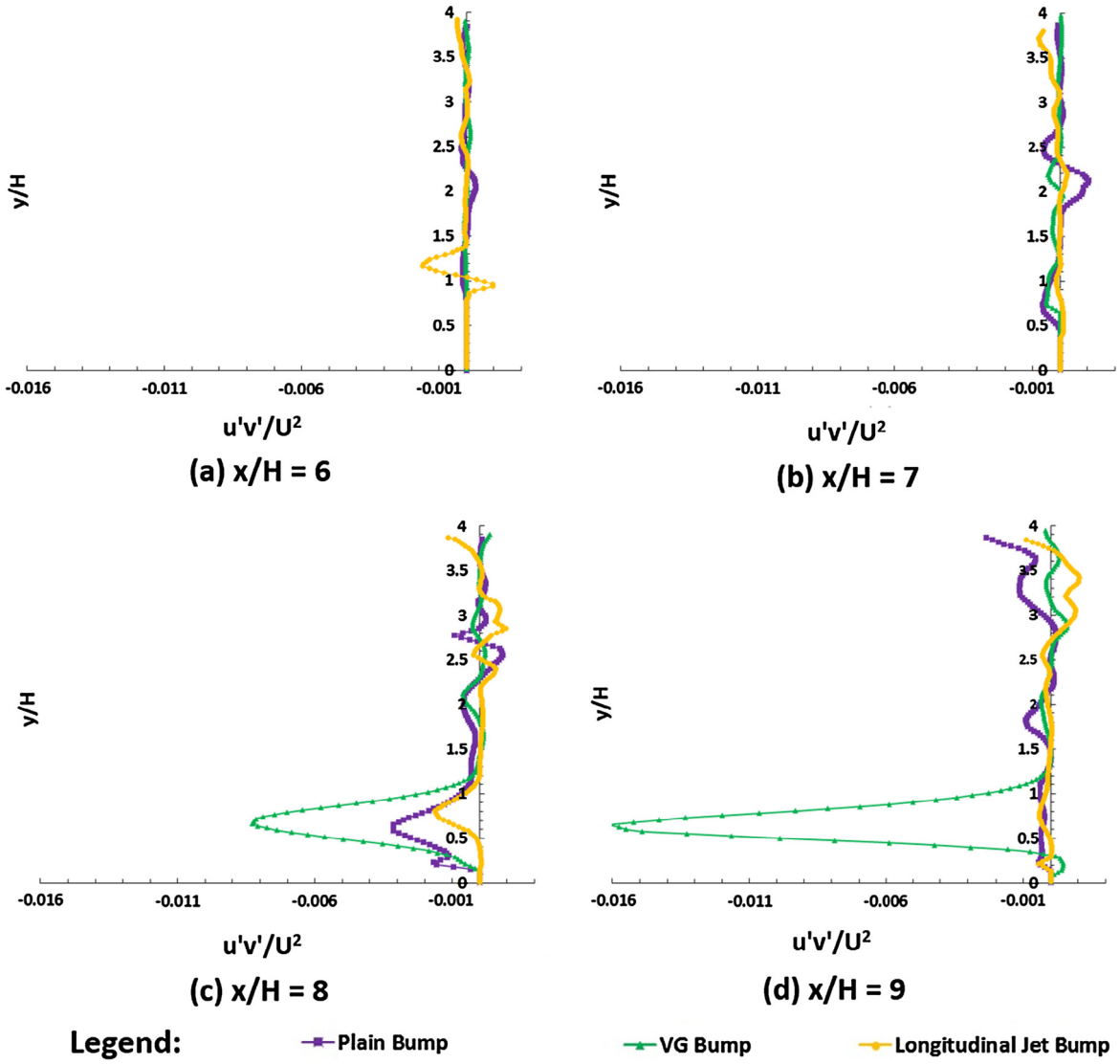

Fig. 12. Normalised Reynolds stress profiles in the xy-plane along the wake region of the (a) plain bump, (b) VG bump and (c) longitudinal jet bump.

mixing enhancement in the VG bump was confirmed when the normalised rms x- and y-velocity profiles and the normalised Reynolds stress profile along the wake region were considered. Also, it was observed that the level of flow mixing increases progressively when the two streamwise horseshoe vortices propagate progressively downstream along the wake region.

In contrast, in the longitudinally jet bump, the passive by-pass jet that blowing in the bump valley increases the flow velocity and momentum of the flow along the wake region. This in-turn increases the capability of the flow to resist the appearance of flow reversal along the wake region of the longitudinal jet bump. In addition, flow stabilisation effects provided by the blowing passive by-pass jet were observed. This effect was confirmed by the presence of relatively low levels of the normalised rms x- and y- velocity and the normalised Reynolds stress along the wake region of the longitudinal jet bump.

Author contributions

All experiments, data processing and analysis were conducted by Kin Hing Lo. Manuscript preparation and editing were conducted by both Kin Hing Lo and Konstantinos Kontis.

Conflicts of interest

The authors declare no conflict of interest.

Acknowledgments

The authors would like to acknowledge Prof. Ning Qin in the University of Sheffield for providing the geometry and design parameters of the optimised three-dimensional rounded contour bump used in the present experimental study. In addition, the authors would like to acknowledge the Engineering and Physical Sciences Research Council – United Kingdom (EPSRC) for funding this research (EPSRC award no.: EPSRC EP/K504488/1).

Appendix A. Detailed geometry and dimensions of the VG bump

Fig. A1

Appendix B. Additional image that shows the spanwise flow pattern over the VG bump

Fig. B1

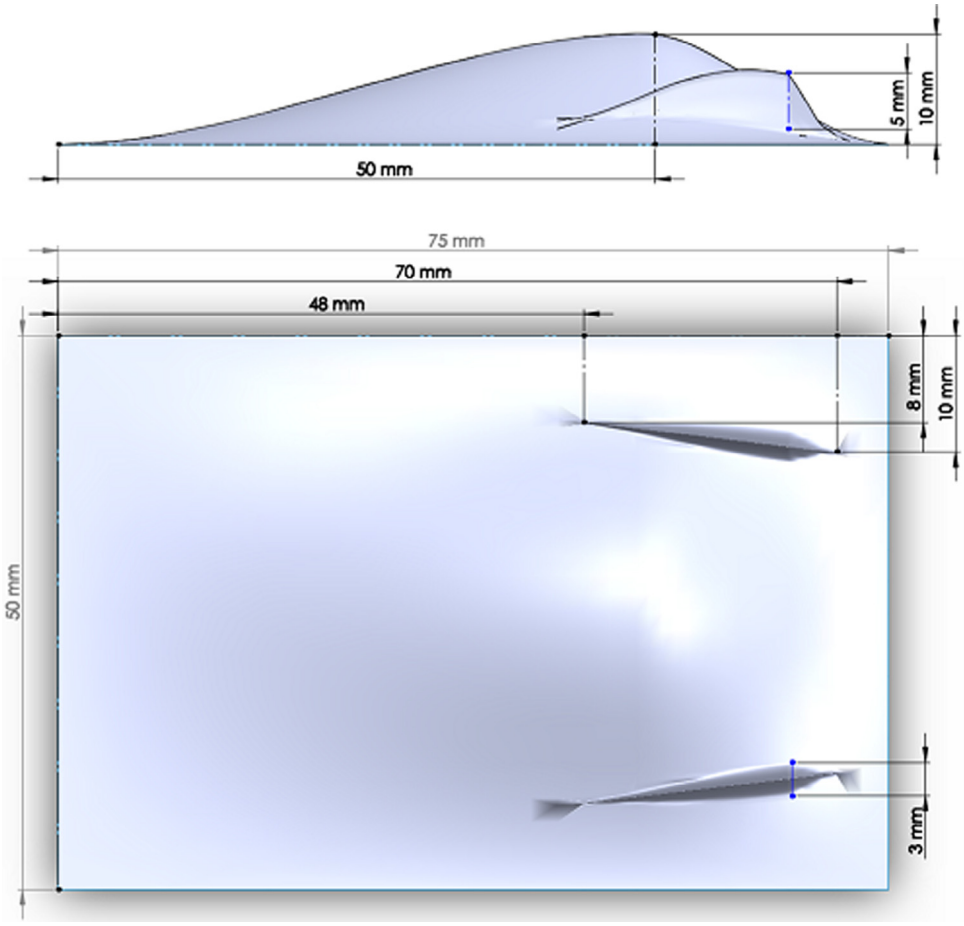

Fig. A1. Schematic of the VG bump that shows detailed geometry and dimensions information.

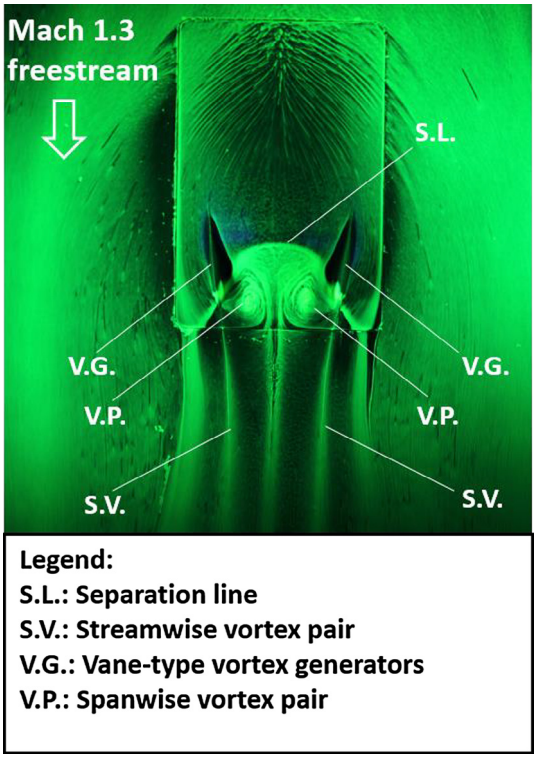

Fig. B1. Spanwise flow pattern over the VG bump obtained from the surface oil flow visualisation experiment using single colour fluorescent oil.

References

[1] G. Byun, Structure of Three-Dimensional Separated Flow on Symmetric Bumps Ph.D. Thesis, Virginia Polytechnic Institute and State University, Blacksburg, Virginia, United States, 2005.
[2] G. Byun, C. Long, R. Simpson, Study of vortical separation from three-dimensional symmetric bumps, AIAA J. 42 (4) (2004) 754–765.
[3] A. Yakeno, S. Kawai, T. Nonomura, K. Fujii, Separation control based on turbulence transition around a two-dimensional hump at different Reynolds numbers, Int. J. Heat Fluid Flow 55 (2015) 52–64.
[4] G. Iaccarino, C. Marongiu, P. Catalano, M. Amato, RANS Simulation of the Separated Flow Over a Bump with Active Control Annual Research Briefs, Centre for Turbulence Research, 2003, pp. 389–397.
[5] K.H. Lo, Experimental Studies on Contour Bumps and Cavities at Supersonic Speed Ph.D. Thesis, University of Manchester, Manchester, United Kingdom, 2014.
[6] K.H. Lo, K. Kontis, Flow characteristics of various three-dimensional rounded contour bumps in a Mach 1.3 freestream, Exp. Therm. Fluid Sci. 80 (2017) 228–243, http://dx.doi.org/10.1016/j.expthermflusci.2016.08.027.
[7] K.H. Lo, H. Zare-Behtash, K. Kontis, Control of flow separation on a contour bump by jets in a Mach 1.9 freestream: an experimental study, Acta Astronaut. 126 (2016) 229–242.
[8] K.H. Lo, K. Kontis, Flow visualisation of a normal shock impinging over a rounded contour bump in a Mach 1.3 free-stream, J. Visual. (2016), http://dx.doi.org/10.1007/s12650-016-0392-4, early online publication.
[9] J.P. Eastwood, J.P. Jarrett, Toward designing with three-dimensional bumps for lift/drag improvement and buffet alleviation, AIAA J. 50 (12) (2012) 2882–2898.
[10] B. König, M. Pätzold, T. Lutz, E. Krämer, Shock control bumps on flexible and trimmed transport aircraft in Transonic Flow, in: New Results in Numerical and Experimental Fluid Mechanics VI, Notes on Numerical Fluid Mechanics and Multidisciplinary Design (NNFM), vol. 96, 2007, pp. 80–87.
[11] B. König, M. Pätzold, T. Lutz, E. Krämer, H. Rosemann, K. Richter, H. Uhlemann, Numerical and experimental validation of three-dimensional shock control bumps, J. Aircraft 46 (2) (2009) 675–682.
[12] N. Qin, W.S. Wong, A. Le Moigne, Three-dimensional contour bumps for transonic wing drag reduction, Proc. IMech E Part G J. Aerosp. Eng. 222 (5) (2008) 619–629.

[13] W.S. Wong, N. Qin, N. Sellars, H. Holden, H. Babinsky, A combined experimental and numerical study of flow structures over three-dimensional shock control bumps, J. Aerosp. Sci. Technol. 12 (2008) 436–447.
[14] P.C. Simon, D.W. Brown, R.G. Huff, Performance of External-Compression Bump Inlet at Mach Numbers of 1.5 and 2.0, NACA Report, NACA-RM-E56L19, 1957.
[15] M. Svensson, A CFD Investigation of a Generic Bump and Its Application to a Diverterless Supersonic Inlet Master Thesis, Linkoping University, Linkoping Sweden, 2013.
[16] W.-L. Chen, D.-L. Gao, W.-Y. Yuan, H. Li, H. Hu, Passive jet control of flow around a circular cylinder, Exp. Fluids 56 (11) (2015) 1–15.
[17] W.-L. Chen, X.-J. Wang, F. Xu, H. Li, H. Hu, A passive jet flow control method for suppressing unsteady vortex shedding from a circular cylinder, ASCE, J. Aerosp. Eng. (2016), http://dx.doi.org/10.1061/(ASCE)AS.194305525.0000661 (Early online publication).
[18] F.K. Lu, Q. Li, Y. Shih, A.J. Pierce, C. Liu, Review of micro vortex generators in high-speed flow, in: Proceedings of 49th AIAA Aerospace Sciences Meeting Including the New Horizons Forum and Aerospace Exposition, Orlando, Florida, United States, 4–7 January 2011, 2011.
[19] T. Herges, E. Kroeker, G. Elliott, C. Dutton, Microramp flow control of normal shock/boundary-layer interactions, AIAA J. 48 (11) (2010) 2529–2542.
[20] J.C. Lin, Review of research on low-profile vortex generators to control boundary layer separation, Prog. Aerosp. Sci. 38 (2002) 389–420.
[21] H. Babinsky, Y. Li, C.W. Pitt-Ford, Microramp control of supersonic oblique shock-wave/boundary-layer interactions, AIAA J. 47 (3) (2009) 668–675.
[22] Q. Li, C. Liu, Declining angle effects of the trailing edge of a microramp vortex generator, J. Aircraft 47 (6) (2010) 2086–2095.
[23] H. Zare-Behtash, K.H. Lo, L. Yang, K. Kontis, Pressure sensitive paint measurements at high Mach numbers, Flow Meas. Instrum. (2017), http://dx.doi.org/10.1016/j.flowmeasinst.2016.02.004 (in press).
[24] K. Kontis, R. An, J.A. Edwards, Compressible vortex-ring interaction studies with a number of generic body configurations, AIAA J. 44 (12) (2006) 2962–2978.
[25] K. Kontis, R. An, H. Zare-Behtash, D. Kounadis, Head-on collision of shock wave induced vortices with solid and perforated walls, Phys. Fluids 20 (1) (2008) 016104.
[26] K. Kontis, C. Lada, H. Zare-Behtash, Effect of dimples on glancing shock wave turbulent boundary later interactions, Shock Waves 17 (5) (2008) 323–335.
[27] L. Yang, H. Zare-Behtash, E. Erdem, K. Kontis, Application of AA-PSP to hypersonic flows: the double ramp model, Sensors Actuat. B: Chem. 161 (1) (2012) 100–107.
[28] M.R. Saad, H. Zare-Behtash, A. Che-Idris, K. Kontis, Micro-ramps for hypersonic flow control, Micromachines 3 (2) (2012) 364–378.
[29] L. Yang, E. Erdem, H. Zare-Behtash, K. Kontis, S. Saravanan, Pressure-sensitive paint on a truncated cone in hypersonic flow at incidences, Int. J. Heat Fluid Flow 37 (2012) 9–21.
[30] H. Zare-Behtash, K. Kontis, N. Gongora-Orozco, K. Takayama, Compressible vortex loops: effect of nozzle geometry, Int. J. Heat Fluid Flow 30 (3) (2009) 561–576.
[31] H. Zare-Behtash, N. Gongora-Orozco, K. Kontis, Effect of primary jet geometry on ejector performance: a cold-flow investigation, Int. J. Heat Fluid Flow 32 (3) (2011) 596–607.
[32] L. Yang, H. Zare-Behtash, E. Erdem, K. Kontis, Investigation of the double ramp in hypersonic flow using luminescent measurement systems, Exp. Therm. Fluid Sci. 40 (2012) 50–56.
[33] T. Ukai, H. Zare-Behtash, E. Erdem, K.H. Lo, K. Kontis, S. Obayashi, Effectiveness of jet location on mixing characteristics inside a cavity in supersonic flow, Exp. Therm. Fluid Sci. 52 (2013) 59–67.
[34] T. Ukai, H. Zare-Behtash, K.H. Lo, K. Kontis, S. Obayashi, Effects of dual jets distance on mixing characteristics and flow path within a cavity in supersonic crossflow, Int. J. Heat Fluid Flow 50 (2014) 254–262.
[35] H. Zare-Behtash, K.H. Lo, K. Kontis, T. Ukai, S. Obayashi, Transverse jet-cavity interactions with the influence of an impinging shock, Int. J. Heat Fluid Flow 53 (2015) 146–155.
[36] W.T. Lusk, Control of Supersonic Cavity Flow by Leading Edge Blowing Master Thesis, University of Florida, United States, 2011.
[37] T. Lusk, J. Dudley, L. Ukeiley, L. Cattafesta, Flow field effects on control on supersonic open cavities, in: Proceedings of 49th AIAA Aerospace Sciences Meeting Including the New Horizons Forum and Aerospace Exposition, Orlando, Florida, United States, 4–7 January, 2011, 2011.
[38] T. Lusk, L. Cattafesta, L. Ukeiley, Leading edge slot blowing on an open cavity in supersonic flow, Exp. Fluid 53 (2012) 187–199.
[39] K.H. Lo, K. Kontis, Flow characteristics over a tractor-trailer model with and without vane-type vortex generator installed, J. Wind Eng. Indust. Aerodyn. 159 (2016) 110–122.
[40] K.H. Lo, K. Kontis, Flow around an articulated lorry model, Exp. Therm. Fluid Sci. 82 (2017) 58–74.